Astronomy & Astrophysics manuscript no. output ©ESO 2024
October 7, 2024

50 Dra: Hump and spike Am-type twins in a non-eclipsing system

M. Skarka[1, 2], J. Lipták[1, 3], E. Niemczura[4], Z. Mikulášek[2], M. Cabezas[1, 3], M. Vítková[1, 2], R. Karjalainen[1], and P. Kabáth[1]

[1] Astronomical Institute of the Czech Academy of Sciences, Fričova 298, CZ-25165 Ondřejov, Czech Republic
e-mail: `skarka@asu.cas.cz`
[2] Department of Theoretical Physics and Astrophysics, Masaryk University, Kotlářská 2, CZ-61137 Brno, Czech Republic
[3] Institute of Theoretical Physics, Faculty of Mathematics and Physics, Charles University, V Holešovičkách 2, 180 00 Praha 8, Czech Republic
[4] Instytut Astronomiczny, Uniwersytet Wrocławski, Kopernika 11, PL-51-622 Wrocław, Poland

Received July xx, 2023; accepted July xx, 2023

ABSTRACT

Context. The interplay between radiative diffusion, rotation, convection, and magnetism in metallic-line chemically peculiar stars is still not fully understood. Recently, evidence has emerged that these effects can work together.
Aims. Our goal is to study the bright binary system 50 Dra, describe its orbit and components, and study additional variability.
Methods. We conducted our analysis using TESS short-cadence data and new high-resolution spectroscopic observations. We disentangled the spectra using KOREL and performed spectral synthesis with ATLAS9 and SYNTHE codes. The system was modelled using KOREL and PHOEBE2.4. We also employed SED fitting in ARIADNE and isochrone fitting using PARAM1.5 codes.
Results. Our findings indicate that the non-eclipsing system (with an inclination of 49.9(8) deg) 50 Dra, displaying ellipsoidal brightness variations, consists of two nearly equal A-type stars with masses of $M_1 = 2.08(8)$ and $M_2 = 1.97(8)\,M_\odot$ and temperatures of 9800(100) and 9200(200) K, respectively. Our analysis also suggests that the system, with an orbital period of $P_{\rm orb} = 4.117719(2)$ days, is tidally relaxed with a circular orbit and synchronous rotation of the components. Furthermore, we discovered that both stars are metallic-line Am chemically peculiar stars with an underabundance of Sc and an overabundance of iron-peak and rare-earth elements. We identified a hump and spike feature in the frequency spectrum with an unusually low frequency of 0.275(2) c/d. According to the current knowledge, this feature should be associated with Rossby modes, spots, and differential rotation in fast rotators. However, the spike frequency does not align with the expected rotation frequency of the stars. This discrepancy may be due to faster rotation of the core, consistent with the theory of overstable convective modes, or it could be attributed to anti-solar differential rotation.
Conclusions. The system 50 Dra exhibits numerous exciting and sometimes contradictory characteristics. All the elements required to explain the hump and spike feature contradict the process of radiative diffusion and warrant further theoretical investigation.

Key words. Stars: variables: general – Stars: chemically peculiar – Binaries: spectroscopic – Stars: rotation – Methods: data analysis

1. Introduction

About a third of spectral A-type stars show a deficiency of He, Ca, and/or Sc an overabundance of iron-group and rare-earths metals (Abt 1981; Gray et al. 2016). These stars, which are mostly observed among stars with spectral type earlier than F2 within a typical temperature range between 7250 and 8250 K (Gray et al. 2016; Qin et al. 2019), are called metallic-line chemically peculiar (CP) stars, shortly AmFm stars. The peculiar chemical composition is enabled by atomic diffusion, which occurs in stars with stable outer layers that transfer energy through radiation (Michaud 1970). This condition is satisfied in slowly rotating stars ($<\simeq 100\,{\rm km\,s^{-1}}$) where rotational mixing is weak (Abt & Morrell 1995; Qin et al. 2021; Trust et al. 2020). It is not surprising that more than 70 % of AmFm stars are found in binary systems, especially those with orbital periods shorter than 20 days, with a peak at around 5 days, where tidal effects slow down the stars' rotation rate (Abt 1961; Abt & Levy 1985; Carquillat & Prieur 2007). It appears that systems with both components being of AmFm type are quite frequent. Catanzaro et al. (2024) studied six eclipsing binaries with AmFm stars and found that four of these systems exhibit the AmFm peculiarity in both primary and secondary components.

Since He is expected to quickly gravitationally settle down in AmFm stars (Charbonneau & Michaud 1991), they have not been expected to pulsate for a long time. However, with the help of ultra-precise space data, it has been discovered that AmFm stars can pulsate as δ Sct pulsators (e.g. Smalley et al. 2017). It was also discovered that the classical opacity κ mechanism in the He II ionization zone is not responsible for the pulsations in AmFm stars. Instead, the pressure modes excited in δ Sct AmFm stars are either caused by the turbulent pressure mechanism in the hydrogen ionization zone (Antoci et al. 2014; Smalley et al. 2017) or by a bump in Rosseland mean opacity resulting from the discontinuous H-ionization edge in bound-free opacity (Murphy et al. 2020).

There is also a long-standing belief that rotationally induced variability can only be observed in CP stars with strong (kG), globally-organized magnetic fields that can stabilize abundance spots (Ap/Bp stars, Preston 1974). However, a recent investigation of an Ap star 45 Her with a magnetic field strength of only 100 G by Kochukhov et al. (2023) questioned the necessity of strong magnetic fields to stabilize the spots. Furthermore, precise space observations have revealed that CP stars without strong magnetic fields (HgMn and AmFm stars) and normal A-type stars also show rotation modulation (e.g. Balona 2011; Sikora et al. 2019; Kochukhov et al. 2021; Trust et al. 2020). The brightness variations in the non-magnetic A-stars are less regular than in magnetic CP stars and resemble differential rotation and spot evolution observed in cool stars (e.g. Balona 2011; Blazère et al. 2020). This observational evidence, combined with rotation periods of less than 1 day observed in some Am and HgMn stars, challenges the notion of requirements for stable and calm atmospheres in these stars (Kochukhov et al. 2007; Trust et al. 2020).

The Fourier spectrum of the data series of many normal and AmFm stars often displays a broad group of close-spaced peaks, followed by a single peak or a very narrow group of unresolved peaks (Balona 2013; Balona et al. 2015; Trust et al. 2020; Henriksen et al. 2023a). The sharp peak (referred to as the 'spike') is believed to be caused by spots and rotation. In contrast, the broad group of peaks (the 'hump') is thought to be due to unresolved Rossby modes mechanically excited by deviated flows caused by stellar spots or mass outbursts, and by non-synchronous tidal forces (Saio et al. 2018).

The nature of the spike feature is still a topic of debate (e.g. Henriksen et al. 2023a,b). According to Cantiello & Braithwaite (2019), bright spots may appear in A-type stars as a result of weak local dynamo-generated magnetic fields in thin (sub)surface H, He, and/or Fe ionization zones where convection can occur. On the other hand, Lee & Saio (2020) and Lee (2021) suggest that overstable convective modes in the core can resonantly excite low-frequency g modes, leading to brightness variations. Both explanations require fast rotation rates of stars and differential rotation. These conditions would prevent radiative diffusion due to chemical mixing and are not expected to be observed in slowly rotating Am stars. The interplay between rotation, (sub)surface convection, magnetism, and radiative diffusion remains an open question.

Our study focuses on a 5.3-mag star 50 Dra (basic parameters in Table 1), which is a double-line spectroscopic binary system. The binary nature of 50 Dra was first discovered by Harper (1919), who found an orbital period of 4.1175 days and estimated the basic parameters of the orbit. Skarka et al. (2022) classified this star as a ROTM|GDOR variable, suggesting variations connected with rotation and/or pulsations. We collected new spectroscopic observations over a century later and found almost the same orbital parameters as Harper (1919). However, a combination of our new spectroscopic observations with photometric data from the TESS mission (Sect. 2, Ricker et al. 2015) allowed us to discover ellipsoidal and additional brightness variations, exhibiting a typical hump and spike pattern (Sect. 3). This enabled us to determine the parameters of the system and both components (Sect. 4), and to reveal that both stars are metallic-line CP stars (Sect. 5). The system of 50 Dra with slowly rotating Am components poses a challenge in explaining the hump and spike feature, as we discuss in Sect. 6.

Table 1. Basic characteristics of 50 Dra.

HD 175286, TIC 424391564, Gaia DR3 2268467486545969792		
ID	Value	Source
$\mathrm{RA}_{\mathrm{J2000}}$ ($^{\mathrm{hh}}:^{\mathrm{mm}}:^{\mathrm{ss}}$)	18:46:22.24	1
$\mathrm{DEC}_{\mathrm{J2000}}$ ($^{\circ}:':''$)	+75:26:02.24	1
Tycho V_T (mag)	5.358(1)	2
Tycho B_T (mag)	5.409(14)	2
TESS T (mag)	5.345 (7)	3
Gaia G (mag)	5.357(3)	4
$\mu_\alpha \cos\delta$ (mas yr^{-1})	17.061(141)	4
μ_δ (mas yr^{-1})	70.391(145)	4
Parallax (mas)	11.415(106)	4
γ (km s^{-1})	-8.79(49)	5
	-7.8	6
	-8.8(2.8)	7
T_{eff} (K)	9150(142)	3
	9572^{+128}_{-297}	4
	9130^{+290}_{-262}	SED
[Fe/H] (dex)	$0.215^{+0.208}_{-0.133}$	4
	$-0.073^{+0.206}_{-0.230}$	SED
$\log g$ (cm s^{-2})	3.966(665)	3
	$3.935^{+0.024}_{-0.028}$	4
	$3.898^{+0.331}_{-0.331}$	SED

Notes. Note: effective temperature T_{eff} and surface gravity $\log g$ corresponds with the assumption of a single star. **References:** 1 – Gaia Collaboration et al. (2021), 2 – Høg et al. (2000), 3 – Paegert et al. (2021), 4 – Gaia Collaboration et al. (2023), 5 – Harper (1919), 6 – Wilson (1953), 7 – Gontcharov (2006), SED – this work (spectra energy distribution fitting).

2. Observations

2.1. TESS photometry

We collected available data reduced by the TESS Science Processing Operations Center (SPOC; Jenkins et al. 2016) and the quick-look pipeline (QLP; Huang et al. 2020a,b) using Lightkurve software (Lightkurve Collaboration et al. 2018; Barentsen & Lightkurve Collaboration 2020) from the MAST archive. We extracted the pre-search data conditioning simple aperture photometry (PDCSAP) flux with long-term trends removed (Twicken et al. 2010) and transformed the normalized flux to magnitudes. The Lightkurve was also used for stitching the data from different sectors together.

Data generated by various pipelines at different cadences exhibit differences. The most reliable products are 2-min (short-cadence, SC) SPOC data sets as discussed by Skarka et al. (2022). The distinctions between the 50 Dra data products are illustrated in Fig. 1. The frequency spectra of the SPOC SC data exhibit the lowest noise level, do not show the artificial peak at 0.07 c/d (as is present in QLP), and the distribution of SC data diminishes the presence of the artificial data peaks, for example, around the dominant frequency peak at 0.48 c/d. Consequently, we opted to base our analysis on the 2-minute SPOC data. We acquired SPOC SC data from 28 sectors (14-26, 40-41, 47-58, 60, and 74), excluding data from sector 25 due to its poor quality. In total, we utilised 440 166 2-min cadence observations spanning almost 4.5 years (1629 days, from 2019-2024).

The contamination ratio of only 0.02 % (Paegert et al. 2021) suggests no contamination of the 50 Dra light. The only possible contaminants are two bright stars 20 and 34 arcmin away[1] and 17 additional faint stars (7.7-12.5-mag fainter than 50 Dra, see Table A.1) near 50 Dra shown in Fig. 2. However, the two bright stars do not show signatures of variability similar to 50 Dra and a custom aperture analysis around the faint numbered stars in Fig. 2 rejects the possibility that any of the signals observed in 50 Dra originates from a different star.

---

[1] HD 174257 ($V = 7.53$ mag) and HD 176795 ($V = 6.71$ mag)

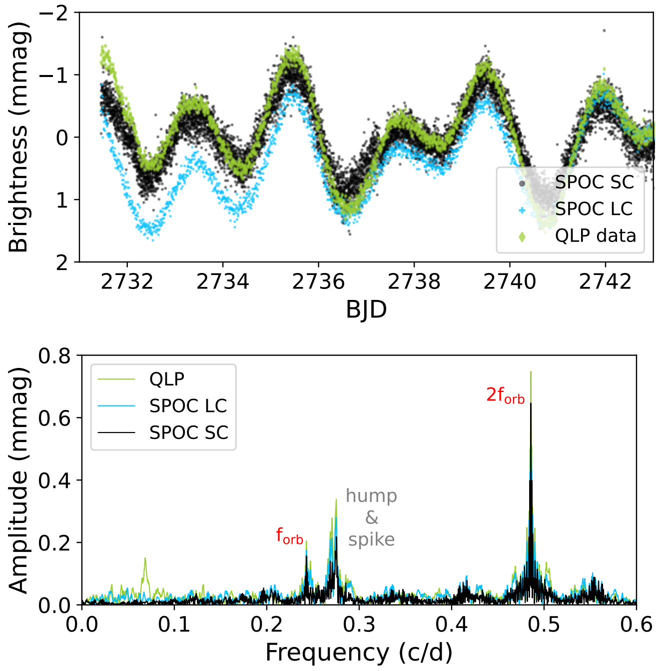

Fig. 1. Comparison of the available data products produced by different pipelines (top panel) and corresponding frequency spectra with labelled features (bottom panel).

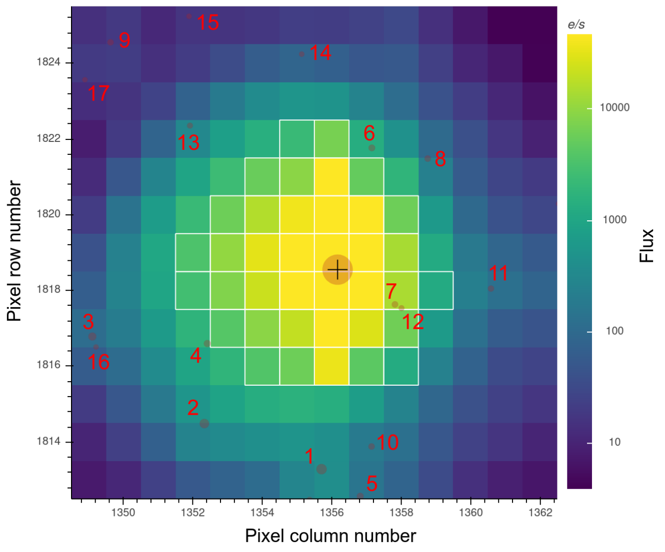

Fig. 2. Vicinity of 50 Dra showing the aperture mask in Sector 14 with the identification of possible contaminants identified in Table A.1 in Appendix. The field size shown in the figure is about 4x4 arcmin.

2.2. Spectroscopy

We obtained 20 spectra of 50 Dra between February and July 2022 using the Ondřejov Echelle Spectrograph (OES) at the 2m Perek telescope (Ondřejov, Czech Republic). The spectrograph has a resolving power of $R = \lambda/\delta\lambda \approx 50\,000$ in the Hα region and covers a spectral range of 3800-9100 Å (Koubský et al. 2004; Kabáth et al. 2020). The spectra were processed and reduced using standard tasks in the Iraf package (Tody 1986), and the cosmic-particle hits were eliminated using the DCR code (Pych 2004). The median S/N of the 600-second exposures in the Hα region was 150, with only four exposures having S/N slightly less than 100, and a few reaching S/N= 230.

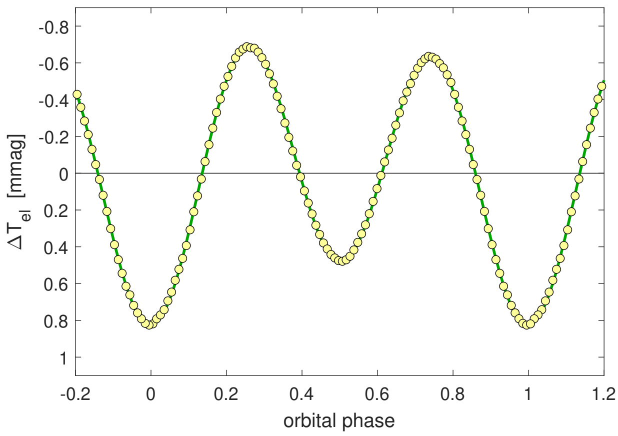

Fig. 3. TESS SC data of 50 Dra phase-folded with the orbital period. Each circle corresponds to a mean of 4 400 individual TESS observations.

3. Photometric variability

We observed the expected double-wave variations in the TESS SC light curve, with a period of $P_{\rm orb} = 4.117719(2)$ days (peaks labelled $f_{\rm orb}$ in Fig. 1). This period agrees with the orbital period derived from spectroscopic observations but is more precise due to a larger time span. As expected, a primary minimum occurs at the inferior conjunction of the binary components.

Given that the orbital period is relatively short and the radial velocity (RV) curves of the components appear almost perfect sinusoids within the observational uncertainties, it is reasonable to assume that the trajectory of the components of the binary star is nearly circular (see Sect. 4, Table 4 and Fig. 7). As a result, the light curve of this non-eclipsing binary, $F_{{\rm ell}(t)}$, can be well approximated by a simple trigonometric polynomial model:

$$F_{\rm ell}(t) = \overline{m} + \sum_{k=1}^{3} A_k \cos(2\pi k\vartheta) - A_4 \sin(2\pi\vartheta), \quad \vartheta = \frac{t - M_0}{P_{\rm orb}}, \quad (1)$$

where t is the BJD timestamp, M_0 is the reference time for the start of the phase that we set at the moment of the inferior conjunction (the time of the deeper minimum). The phase function ($\vartheta(t)$) is the sum of the number of orbits completed by the system since the passage through the basic inferior conjunction, and the fractional orbital phase $\varphi = {\rm Frac}(\vartheta)$. The coefficients of the model are denoted as A_1, A_2, A_3, A_4, and $\overline{m}$. The figure displaying the binned data along with the model is shown in Fig. 3.

Symmetrical terms of the ellipsoidal variability correspond to the effects of tidal deformation of components and reflection, while the anti-symmetrical term, causing the uneven heights of maxima, is the consequence of the Doppler beaming (e.g. Zucker et al. 2007). Parameters of the model with Eq. 1 are in Table 2.

After removing the variability linked to the orbital period $P_{\rm orb} = 4.117719$ days, a complex variability ranging from 0.25 and 0.3 c/d remains in the frequency spectrum (see Fig. 1 and 4). This is a signature of semi-regular variability commonly observed also in hot stars and is believed to be caused by differential rotation and evolution of the surface spots induced by (sub)surface convection (e.g. Balona 2011; Reinhold & Gizon 2015; Trust et al. 2020). Additionally, this pattern is similar to

Table 2. Model parameters of the ellipsoidal variations.

Ephemeris	Parameters
$M_0 = 2\,459\,365.9508(2)$	$A_1 = 0.172\,8(5)$ mmag
$P_{\rm orb} = 4\overset{\rm d}{.}117\,719(2)$	$A_2 = 0.652\,9(4)$ mmag
	$A_3 = 0.002\,9(4)$ mmag
$\mathrm{ampl}_{\rm eff} = 1.35$ mmag	$A_4 = 0.029\,6(5)$ mmag

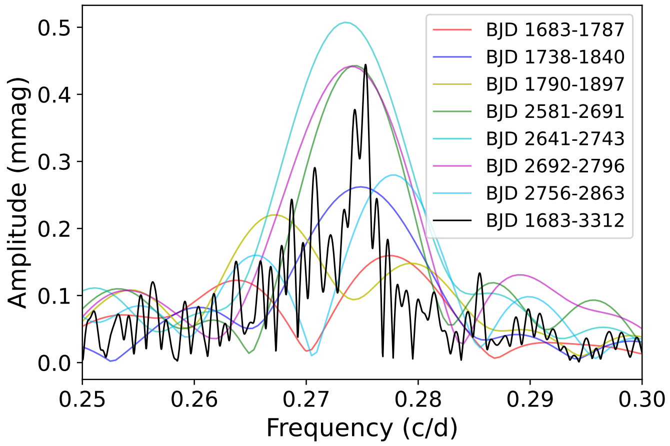

Fig. 4. Frequency spectra around the hump and spike feature corresponding to different data segments (colour lines) and the full data set (black line). The amplitude of the Frequency spectrum of the full dataset is multiplied by two for better readability.

the variability seen in the hump and spike stars (e.g. Balona 2013; Balona et al. 2015; Saio et al. 2018). The group of peaks referred to as 'hump' that precedes the well-defined peak(s) termed 'spike' are thought to be Rossby modes, while the spike is attributed to rotation (Saio et al. 2018; Henriksen et al. 2023a). Further discussion on this feature is provided in Sect. 6.1.

To show how the additional variations with frequencies around 0.27 c/d change over time, we divided the SC time series into 7 segments, each with approximately 100 days of continuous data. These segments overlap by approximately 50 days. The Fourier transform of the data segments is displayed with colour lines in Fig. 4. In addition, we found significant peaks around the harmonics of the spike feature, approximately at 0.55 c/d. Apart from the peaks caused by the ellipsoidal variability and the hump and spike feature, we did not find any other significant peaks. Although the frequencies in the hump and spike region are mostly unresolved, we have included all the detected frequencies in Table A.2 in the Appendix for the sake of completeness.

4. System parameters

4.1. Spectral energy distribution

We used photometry in 12 photometric filters in visual to infrared wavelengths (Table A.3 in Appendix) and fitted the spectral-energy distribution (SED) with ARIADNE (Vines & Jenkins 2022). This code uses SED fitting methods, and Gaia distances, and combines results via Bayesian model averaging to derive basic stellar parameters such as $T_{\rm eff}$, $\log g$, iron abundance [Fe/H], extinction, and radius of a star.

The results of the SED fitting are shown in Fig. 5 and the values we obtained are shown in Table 1 (label 'SED' in the column 'Source'). The results are given only for reference since 50 Dra is not a single star. However, this exercise gives a good idea about the reliability of the stellar parameters from the literature when considering 50 Dra as a single object. The temperature $T_{\rm eff}$= 9123 K, [Fe/H]= −0.073 dex and $\log g = 3.898$ are within their errors consistent with the catalogue values, especially $T_{\rm eff}$ is in excellent agreement with the value from Paegert et al. (2021). The biggest difference is in the iron abundance which is about 0.3 dex lower than [Fe/H] from Gaia Collaboration et al. (2023) and from our spectroscopic analysis (see Sect. 5). Thus, the [Fe/H] form SED is less reliable than from other methods. We will use the radius $R_* = 2.91(9)\,R_\odot$ derived using ARIADNE under the single star assumption to derive the radii of the components in Sect. 4.4.

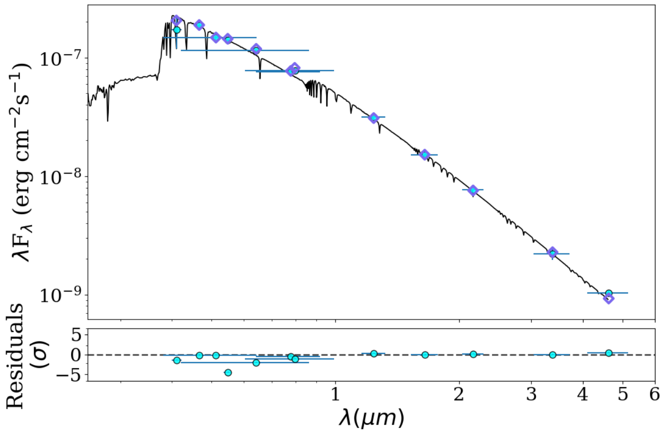

Fig. 5. The spectral-energy-distribution function based on the photometric observations (Table A.3) from ARIADNE.

4.2. Spectra disentanglement

Since 50 Dra is an SB2 binary system, the variations in the position of the spectral lines of both components are distinct and apparent at first glance (see Fig. 6). The movement of some of the prominent spectral lines during the orbital motion is best seen from the trail plots shown in the bottom part of Fig. 6. We used the KOREL code (Hadrava 1995, 2004) for the Fourier spectral disentangling. This code performs simultaneous decomposition of spectra and solution of orbital parameters. We fixed the orbital period $P = 4.117719$ days since it has been precisely determined from the ellipsoidal variations detected in the photometric observations with a time span of almost 4.5 years (Sect. 3).

We performed the Fourier spectral disentangling in 41 spectral regions with a typical width of 140 Å. An example of the final disentangled spectra of both components around the Mg I 5167-5183 Å triplet is shown in detail in the top part of the top panel of Fig. 6. In the end, we decided to use only 25 spectral regions with a sufficient number of spectral lines to get reasonable results that were, in addition, consistent with each other. KOREL also produces RVs and provides a model of the orbit (see Sect. 4.3 and Table 4). The RV values for both components are in Table 3 together with their errors calculated as the standard deviation of the values from the individual segments.

4.3. Orbital parameters

The estimation of the orbital parameters (time of periastron passage T_0, eccentricity e, argument of pericentre ω, semi-amplitudes of radial velocities K_1, K_2, and mass ratio $q = M_2/M_1$) comes from the disentangling process with KOREL when

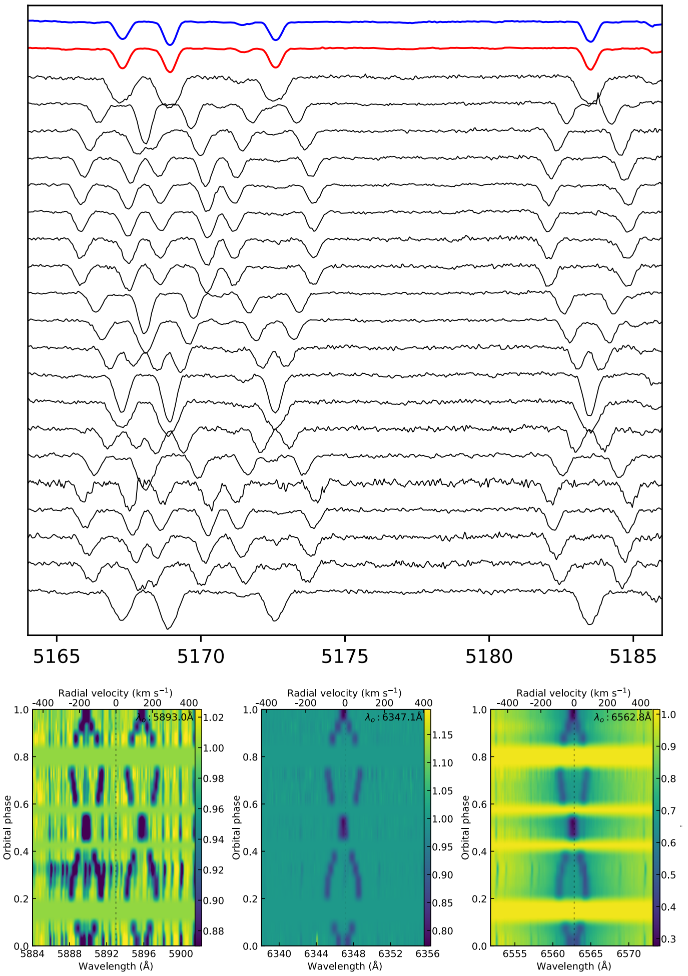

Fig. 6. *(Top)* Observed spectra in different orbital phases around the Mg I 5167-5183 Å triplet and Fe II 5169 Å lines. The two upper-most spectra show the mean disentangled spectra for the primary (blue) and the secondary component (red). *(Bottom)* Trails of Na D, Si II, and Hα lines (from left to right) showing the variation of the position of the lines of both components during the orbital cycle. The relative intensity of the lines is also indicated.

the orbit is simultaneously solved for all the disentangled regions. The values in Table 4, which are calculated as the average values from all the solutions in 25 spectral regions, signalize circular orbit (e is almost zero) with large semi-amplitudes of the radial-velocity (RV) curves ($K_1 \approx 79\,\mathrm{km\,s^{-1}}$, $K_2 \approx 83\,\mathrm{km\,s^{-1}}$). The similarity of the semi-amplitudes and, thus, the mass ratio $q \approx 0.95$, show that both components are almost of equal masses (see Fig. 7). Systems with $q \simeq 1$ components are commonly observed among AmFm binaries as was observed, for example, by Carquillat & Prieur (2007) who found that six of twelve of their SB2 systems have $q > 0.9$. It is worth noting that all our values are consistent with what was estimated more than a hundred years ago by Harper (1919).

The only discrepancy between our results and literature values is the systemic velocity γ. Our value $\gamma = -6.53(9)\,\mathrm{km\,s^{-1}}$ is about 1-2 $\mathrm{km\,s^{-1}}$ larger than the literature values (see Table 1). We did not identify any problem in our analysis that can explain the difference. Since all the previous values are based on low-resolution spectroscopy and/or on photographic plates taken a long time ago, we assume that our new value is of better reliability than those published previously.

Table 3. Radial velocities of both components in $\mathrm{km\,s^{-1}}$.

BJD	RV_1	σ_{RV_1}	RV_2	σ_{RV_2}
2459623.2165	-10.95	0.65	10.45	0.57
2459624.2168	77.53	0.48	-81.65	0.45
2459625.2641	11.68	0.67	-12.41	0.54
2459630.2691	-73.43	0.34	77.75	0.35
2459638.3844	-67.18	0.38	71.13	0.38
2459639.5434	-26.94	0.51	28.70	0.46
2459640.6760	77.22	0.36	-81.54	0.41
2459641.4470	44.24	0.55	-46.18	0.65
2459646.5317	-60.81	0.67	64.68	0.46
2459647.4978	-55.29	0.46	58.77	0.43
2459648.4501	48.68	1.35	-51.43	0.67
2459652.4616	38.66	0.71	-39.85	0.84
2459653.4062	73.58	0.38	-76.96	0.41
2459658.3811	-9.75	0.67	9.12	0.60
2459659.3145	-78.72	0.33	83.21	0.39
2459660.3422	-4.29	1.62	2.26	0.56
2459661.3819	78.90	0.23	-82.76	0.34
2459722.3264	23.24	0.47	-24.11	0.72
2459764.4223	78.18	0.68	-82.31	0.62
2459789.4843	61.93	0.95	-64.85	0.51

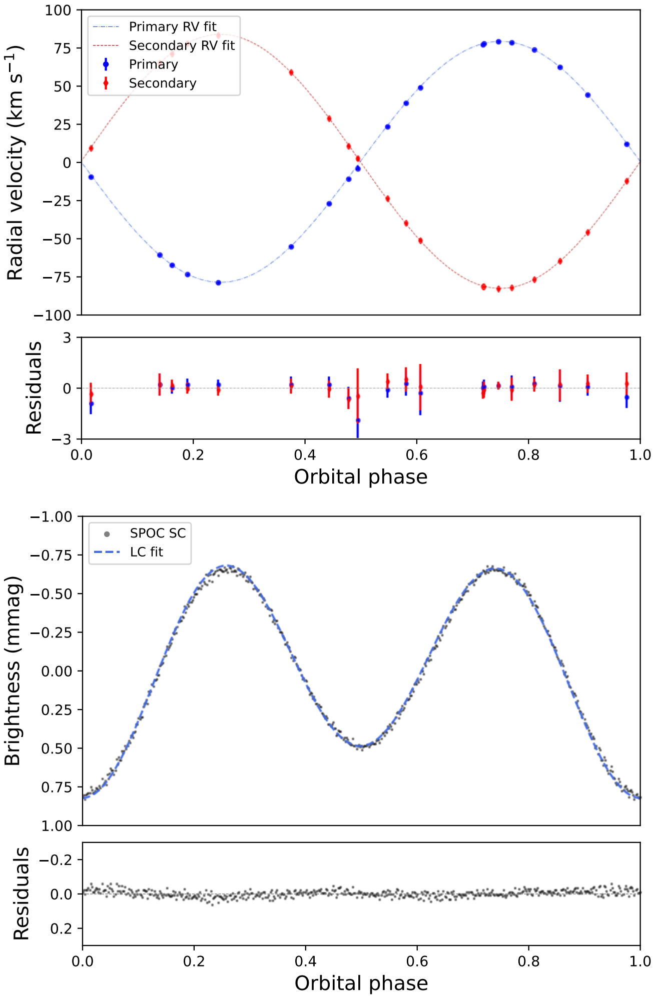

Fig. 7. Radial velocity curve of both components with the best fit (upper panel) and the light curve with the best fit (bottom panel). The photometric points are binned to have 500 points per orbital phase.

Table 4. Parameters of the binary system.

	Korel	H19		Param 1.5	Phoebe 2.4
T_0	2459654.241(4)		M_1 ($M_\odot$)	$2.39^{+0.27}_{-0.15}$	2.08(8)
e	0.0021(3)	0.012(9)	R_1 ($R_\odot$)	$2.13^{+0.80}_{-0.32}$	2.06(9)
ω (deg)	94.85(2)		$(\log g)_1$ (cm s^{-2})	$4.16^{+0.23}_{-0.11}$	4.13(5)
K_1 (km s^{-1})	78.93(2)	79.12(97)	M_2 ($M_\odot$)	$2.21^{+0.15}_{-0.13}$	1.97(8)
K_2 (km s^{-1})	82.96(20)	83.9(97)	R_2 ($R_\odot$)	$2.34^{+0.35}_{-0.30}$	1.99(9)
$q(M_2/M_1)$	0.951(2)	0.947	$(\log g)_2$ (cm s^{-2})	$4.04^{+0.10}_{-0.10}$	4.13(5)
$a \sin i$ ($R_\odot$)		13.3	$a \sin i$ ($R_\odot$)		13.184(26)
i (deg)			i (deg)		49.9(8)

Notes. H19 is the reference to Harper (1919).

4.4. Characteristics of the system components

As a proxy, we estimated stellar parameters using the Bayesian fitting tool PARAM 1.5[2] (da Silva et al. 2006; Rodrigues et al. 2014, 2017). The code uses a new version of PARSEC (Bressan et al. 2012) evolutionary tracks and isochrones that include effects of rotation, improvements in nuclear reaction network and other effects (Nguyen et al. 2022). Since 50 Dra is not a single star, we had to calculate the observed magnitudes for each component.

If we assume the mass ratio $q \approx 0.951$ and the mass-luminosity relation $L \simeq M^{4.329}$ for the main-sequence stars in the 1.05–2.4$M_\odot$ range (based on 275 well measured stars, Eker et al. 2018), we get the flux ratio $F_{\rm Prim}/F_{\rm Sec} = 0.951^{-4.329} = 1.243$. After transformation into magnitudes, we end up with $V_{\rm Prim} = 5.997$ mag and $V_{\rm Sec} = 6.238$ mag by assuming the total magnitude of the system $V_T = 5.358$ mag (Høg et al. 2000). We used the calculated V magnitudes, $T_{\rm eff}$, $\log g$ and [Fe/H] from Table 5, and Gaia DR3 parallax from Table 1 as the input parameters for Param 1.5. Although being only rough estimates, the resulting values (see Table 4) are all within errors consistent with results from binary star modelling and spectral analysis (Sect. 5).

As an alternative and more appropriate way of deriving the system parameters without using stellar evolution models, we use the light-curve model, SED fit, and radial velocities. We use Phoebe 2.4 (Conroy et al. 2020) to run the binary model. Since the Doppler beaming, apparent in our light curve, is not currently implemented in Phoebe 2.4 and the use of SED is quite convoluted, we turn to a direct computation of radii and temperatures.

The Doppler beaming amplitude is given by

$$\frac{\Delta F}{F} = \frac{1}{c}\frac{\beta_1 K_1 F_1 - \beta_2 K_2 F_2}{F_1 + F_2}\,. \tag{2}$$

Using the radial velocity amplitudes from Korel and beaming coefficients $\beta_1 = 2.01(5)$, $\beta_2 = 2.09(5)$ derived by interpolation from tables by Claret et al. (2020) for TESS passband we get the passband relative fluxes $F_1/(F_1 + F_2) = 0.547(9)$ and $F_2/(F_1 + F_2) = 0.453(9)$. Next, we use Phoebe to derive the relation between the flux and temperature ratios for the stars with the same radius $R_1 = R_2 = 2R_\odot$ in the TESS passband. Using the range $T_2/T_1 \in (0.90, 1.00)$ and primary star temperature $T_1 = 9800\,K$ we get a linear relation between the two. After adding the factor of the ratio of surface areas we come to the final relation

$$F_2/F_1 = \left(-0.88 + 1.88\frac{T_2}{T_1}\right)\left(\frac{R_2}{R_1}\right)^2\,. \tag{3}$$

To get the radii themselves, we use the SED result for R_*. In the long wavelength limit (far IR) under the Raighley-Jeans approximation it should hold

$$R_1^2 T_1 + R_2^2 T_2 = R_*^2 T_*\,, \tag{4}$$

where R_*, and T_* are the stellar radius and effective temperature derived in the single star assumption in Sect. 4.1. Using the effective temperatures of stars $T_1 = 9800(100)\,K$ and $T_2 = 9200(200)\,K$ derived from spectra (see Sect. 5) we get the radii $R_1 = 2.06(9)$ and $R_2 = 1.99(9)$.

Next, we can fit the ellipsoidal variation in PHOEBE to get the inclination of the system. We use PHOENIX atmospheric models by Husser et al. (2013) to get the passband luminosities and limb-darkening coefficients. We set bolometric gravity brightening coefficients of both stars $b_1 = b_2 = 1.0$ and bolometric reflection coefficients to $a_1 = a_2 = 1.0$ valid for stars above $T_1 = 8000\,K$ with radiative atmospheres (see Claret (2003)). Sampling the derived radii-temperature distributions we get the inclination of $i = 49.9(8)$ deg. This finally allows us to derive the semimajor axis of the system and masses of the components from the radial velocity fit. The best fit (shown in Fig. 7) gives values shown in the last column in Table 4. All the parameters obtained with Phoebe are in line with the results from other routines and methods.

5. Spectral synthesis and abundances

Before the analysis of the spectra, we scaled the disentangled spectra of both components assuming the flux ratio of $F_1/F_2 = 1.243$ (based on empirical formulae from Eker et al. 2018) meaning that $F_1 = 0.555\,{\rm F_{tot}}$ and $F_2 = 0.445\,{\rm F_{tot}}$ which are in agreement with flux ratios calculated from the Doppler beaming amplitudes (Sect. 4.4). We used the spectrum synthesis method to analyze the spectra of both stars. This method allows for the simultaneous determination of parameters influencing stellar spectra and involves minimizing the deviation between theoretical and observed spectra. The synthetic spectrum depends on stellar parameters such as effective temperature ($T_{\rm eff}$), surface gravity ($\log g$), microturbulence ($V_{\rm mic}$), projected rotational velocity ($V \sin i$), and the relative abundances of the elements ($\log N$(El)), where 'El' denotes the individual element. All these parameters are correlated.

All the necessary atmospheric models were computed with the line-blanketed, local thermodynamical equilibrium (LTE) ATLAS9 code whereas the synthetic spectra were computed with the SYNTHE code (Kurucz 2005). Both codes, ATLAS9 and SYNTHE, were ported to GNU/Linux by Sbordone (2005). The stellar line identification and the abundance analysis over the

---

[2] `http://stev.oapd.inaf.it/cgi-bin/param`

entire observed spectral range were performed based on the line list from the Fiorella Castelli website[3]. The solar abundances were adopted from Asplund et al. (2005).

In our method, effective temperature, surface gravity and microturbulence were obtained from the analysis of lines of neutral and ionised iron. We adjusted $T_{\rm eff}$, $\log g$ and $V_{\rm mic}$ by comparing the abundances determined from Fe I and Fe II lines. First, we adjusted $V_{\rm mic}$ until we saw no correlation between iron abundances and line depths for the Fe I lines. Next, we changed $T_{\rm eff}$ until there was no trend in the abundance versus excitation potential for the Fe I lines. Then, surface gravity was obtained by fitting the Fe II and Fe I lines, ensuring the same iron abundances from the lines of both ions. With the derived $T_{\rm eff}$, $\log g$, and $V_{\rm mic}$, the determination of abundances was performed. The final results are presented in the Table 5. The errors of chemical abundances given in Table 5 are standard deviations resulting from the analysis of many spectral lines of a given element or result from the steps in the grid of calculated atmospheric models.

i pochválit Emu, je šikovná. Pro zpracování pozorovacího materiálu má buňky, na konzultace bývá dobře připravená.

The derived atmospheric parameters and chemical abundances are influenced by errors from several sources, e.g. assumptions taken into account to build an atmospheric model, the adopted atomic data, and spectra normalization. A detailed discussion of possible uncertainties of the obtained parameters is given in Niemczura et al. (2015) and Niemczura et al. (2017). The comparison of the exemplary observed and theoretical spectra calculated for the final parameters is shown in Fig. 8.

The effective temperatures of both components ($T_{\rm eff\,1}$ = 9800(100) K and $T_{\rm eff\,2}$ = 9200(200) K) and their surface gravities (($\log g)_1$ = 4.1(1) and $(\log g)_2$ = 4.0(1) cm s^{-2}) suggest that both stars are of A0-A3 V spectral types. Both system components are slow-rotators with $v \sin i$= 19(1) km s^{-1}, which is significantly less than is typical for most of the A-type stars (150-200 km s^{-1}, Zorec & Royer 2012).

We estimated abundances for 29 elements (see Table 5). The number of lines used for the abundance estimation is given in columns denoted as 'Nr'. It is seen that Fe abundance is the most robust value based on 207 and 206 spectral lines for the primary and secondary components, respectively. The iron abundance is slightly different for both components ($[{\rm Fe/H}]_{\rm prim}$ = 0.21(9) and $[{\rm Fe/H}]_{\rm sec}$ = 0.08(10)) but they are consistent within their errors. Both [Fe/H] values are in line with the catalogue value (Gaia Collaboration et al. 2023) but are about 0.3 dex higher than the values from the SED fitting (Sect. 4). The abundances of iron-peak and Earth-rare elements together with slow rotation suggest the chemical peculiarity of both components as discussed in Sect. 6.2.

6. Discussion

6.1. Rotation and the hump and spike feature

At first glance, rotation velocity of the components $v_{\rm rot,1,2}$ = $v \sin i / \sin i \approx 24.8$ km s^{-1} (see Table 4) is not special among A-type stars because the distribution of the rotational velocities for slowly-rotating normal A-type, CP and stars in close binary systems overlap (e.g. Royer et al. 2007). However, the rotational velocity of both components is lower than the average velocity of A and Am stars (161 ± 3 and 105 ± 3 km s^{-1} Trust et al. 2020), (86.8 and 33.4 km s^{-1} Qin et al. 2021) showing that the rotation of 50 Dra components is, actually, very slow compared to other A-type stars.

If we assume values of $R_{1,2}$, $(v \sin i)_{1,2}$, and i from Table 4 and calculate rotation frequencies of both components $f_{\rm rot,1,2}$ by solving a commonly used relation for the rotation period (e.g. Preston 1971)

$$f_{\rm rot} = \frac{v \sin i}{50.6 R_* \sin i}, \tag{5}$$

we end up with rotational frequencies of the two components $f_{1,\rm rot}$ = 0.238(17) and $f_{2,\rm rot}$ = 0.246(17) c/d. Both values are consistent with the orbital frequency $f_{\rm orb}$ = 0.2428529(1) c/d. This simple exercise suggests that the value of the inclination is well established and that the system is relaxed with a circularized orbit and synchronous rotation of the components. The assumption of circular orbit and synchronously rotating components is further reinforced by the following angular momentum investigation.

The tidal equilibrium of the system is only possible if the total angular momentum of the system $L_{\rm tot}$ (a sum of the orbital and spin momenta) is larger than a critical momentum $L_{\rm crit}$ that can be calculated following Ogilvie (2014) as

$$L_{\rm crit} = 4I(GM)^{1/2} \left(\frac{\mu}{3I}\right)^{3/4}, \tag{6}$$

where $M = M_1 + M_2$ is the total mass of the stars (values from Phoebe in Table 4), $I = I_1 + I_2$ is the total spin momentum of inertia of the stars, and $\mu = M_1 M_2/(M_1 + M_2)$. The spin moment of inertia of the stars was calculated as $I = \beta^2 M_* R_*^2$ with M_* and R_* from Table 4 and $\beta = 0.218$ for stars with $M = 2\,M_\odot$ from Claret & Gimenez (1989).

The total angular momentum of the system $L_{\rm tot}$

$$L_{\rm tot} = L_{\rm orb} + L_{\rm spin} = L_{\rm orb} + I_1\Omega_1 + I_2\Omega_2 \tag{7}$$

is dominated by the orbital angular momentum $L_{\rm orb}$ that can be expressed in a form of

$$L_{\rm orb} = \frac{G M_1 M_2 \left(1 - e^2\right)^{1/2}}{\Omega a}, \tag{8}$$

where $\Omega = 2\pi f_{\rm orb}$ rad s^{-1} is the angular velocity. If we assume that the spin angular velocity of the stars equals the orbital angular velocity (the calculated rotational frequencies match the orbital frequency), the $L_{\rm orb} \approx 380 L_{\rm spin}$. The total angular momentum $L_{\rm tot} \sim 2.5 L_{\rm crit}$ means that the system is in tidal equilibrium. At the same time, $L_{\rm orb} \gg 3 L_{\rm spin}$ that means that the system is relaxed with a stable tidal equilibrium resulting in circularized orbit and synchronous rotation of the components (Hut 1980; Ogilvie 2014). Carquillat & Prieur (2007) found that the cut-off orbital period for AmFm stars to be circularized is 5.6(5) days ($f_{\rm orb} \geq 0.179$ c/d).

All the indices we have pointed towards the synchronous rotation of 50 Dra components with the orbital frequency 0.243 c/d. However, the Gaussian fit of the spike structure, between 0.272 and 0.28 c/d based on the full data set (black line in Fig. 4), that is supposed to be caused by rotation (Balona 2013; Balona et al. 2015), gives the frequency of 0.275(2) c/d.[4] This value is more than 3σ larger than the orbital frequency and suggests the non-synchronous rotation of one of the components.

Since both components are almost equal, it is difficult to assign the hump and spike feature to one of the stars and make a proper interpretation. The rotation frequency of the secondary, less massive and smaller component, is closer to the

---

[3] `https://wwwuser.oats.inaf.it/fiorella.castelli/`

[4] The peak at 0.286 c/d can be possibly also considered as the spike.

Table 5. Parameters of the components and their abundances from the spectral synthesis.

	Star 1			Star 2			
$T_{\rm eff}$ (K)	9800(100)			9200(200)			
$\log g$ (cm s^{-2})	4.1(2)			4.0(1)			
$V_{\rm mic}$ (km s^{-1})	0.5(3)			0.5(3)			
$v \sin i$ (km s^{-1})	19(1)			19(1)			
El	Nr	$\log \epsilon$	σ	Nr	$\log \epsilon$	σ	$\log \epsilon$ (Sun)
C	15	8.17	0.25	15	8.12	0.24	8.43
N	4	8.08	0.35	7	8.17	0.16	7.83
O	8	8.52	0.18	6	8.82	0.18	8.69
Ne	-	-	-	1	9.07	0.00	7.93
Na	4	6.88	0.22	1	6.28	0.00	6.24
Mg	9	7.46	0.23	8	7.24	0.06	7.60
Al	2	6.42	0.00	3	6.38	0.11	6.45
Si	11	7.50	0.23	15	7.55	0.26	7.51
P	1	6.26	0.00	2	6.36	0.00	5.41
S	9	7.75	0.19	12	7.66	0.17	7.12
Ca	12	6.28	0.10	13	6.03	0.14	6.34
Sc	5	2.51	0.11	7	2.33	0.38	3.15
Ti	42	5.14	0.12	39	4.94	0.15	4.95
V	8	4.43	0.06	8	4.56	0.31	3.93
Cr	55	6.09	0.13	66	5.93	0.16	5.64
Mn	16	5.76	0.14	24	5.65	0.12	5.43
Fe	207	7.71	0.09	206	7.58	0.10	7.50
Co	1	5.43	0.00	4	5.63	0.24	4.99
Ni	34	6.85	0.11	44	6.69	0.14	6.22
Cu	2	4.89	0.00	2	4.64	0.00	4.19
Zn	1	5.51	0.00	2	5.14	0.00	4.56
Sr	1	3.89	0.00	2	3.47	0.00	2.87
Y	6	3.15	0.09	11	3.07	0.15	2.21
Zr	5	3.68	0.19	16	3.40	0.10	2.58
Ba	4	3.59	0.04	3	3.27	0.00	2.18
La				1	2.37	0.00	1.10
Ce	1	3.17	0.00	7	2.54	0.20	1.58
Nd	1	2.62	0.00	2	2.33	0.00	1.42
Sm				1	1.95	0.00	0.96

Notes. The 'Nr' gives the number of lines used to calculate abundance (including blends), $\log \epsilon$ gives the average abundances (on the scale in which $\log \epsilon(\mathrm{H}) = 12$), σ gives the standard deviation in case that the fit was based on more than three lines, $\log \epsilon$ (Sun) gives the solar abundance (Asplund et al. 2009).

spike frequency suggesting that the signal can originate from the secondary. On the other hand, the synchronisation would take more time in the more massive component. Nevertheless, from the above discussion, there is no reason to consider the non-synchronous rotation of any of the components.

Saio et al. (2018) associated the hump in the frequency spectra with unresolved Rossby modes excited by deviated flows caused stellar spots represented as the rotational peak (the spike). The unresolved peaks in the spike are then interpreted as a result of a differential rotation. In A-type stars, distinct temperature spots are not expected much due to the lack or absence of large convective zones. However, Cantiello & Braithwaite (2019) demonstrated that spots can be induced by local magnetic fields generated by convection in thin (sub)surface zones due to high opacity and/or low adiabatic gradient in the ionization zones of H, He, and/or Fe (Cantiello & Braithwaite 2019).

These magnetic spots are expected to be of low contrast in the order of 10 K and should be mostly undetectable in the majority of A-type stars. In addition, fast rotation of a star and the presence of differential rotation are required to grow the magnetic field to scales larger than the scale of convective motions (Cantiello & Braithwaite 2019; Henriksen et al. 2023a). This condition is not fulfilled in AmFm stars, which have had to avoid rotational mixing to become AmFm stars. However, there are a few AmFm stars where a weak magnetic field was detected (e.g. Blazère et al. 2016a,b). Particularly, components of 50 Dra are very similar to Sirius A, which is also an AmFm star, where a very weak magnetic field of the size of 0.2 ± 0.1 G was detected (Petit et al. 2011), giving a chance that this mechanism could work also in 50 Dra. Nevertheless, only precise measurements of the magnetic field in 50 Dra and detail modelling can answer whether this scenario is the correct one.

Lee & Saio (2020) and Lee (2021) introduced an alternative theory of rotational modulation, which suggests that low-frequency g modes resonantly excited by overstable convective modes in the core can cause variations in brightness in fast-rotating stars when there is differential rotation. This model only applies when the core rotates slightly faster than the envelope. The spike in frequency spectra would then reflect the rotation rate of the core, with the frequency of the spike corresponding to m-times the core rotation rate, where m is the azimuthal order of the g mode (Lee & Saio 2020; Lee 2021). This could ex-

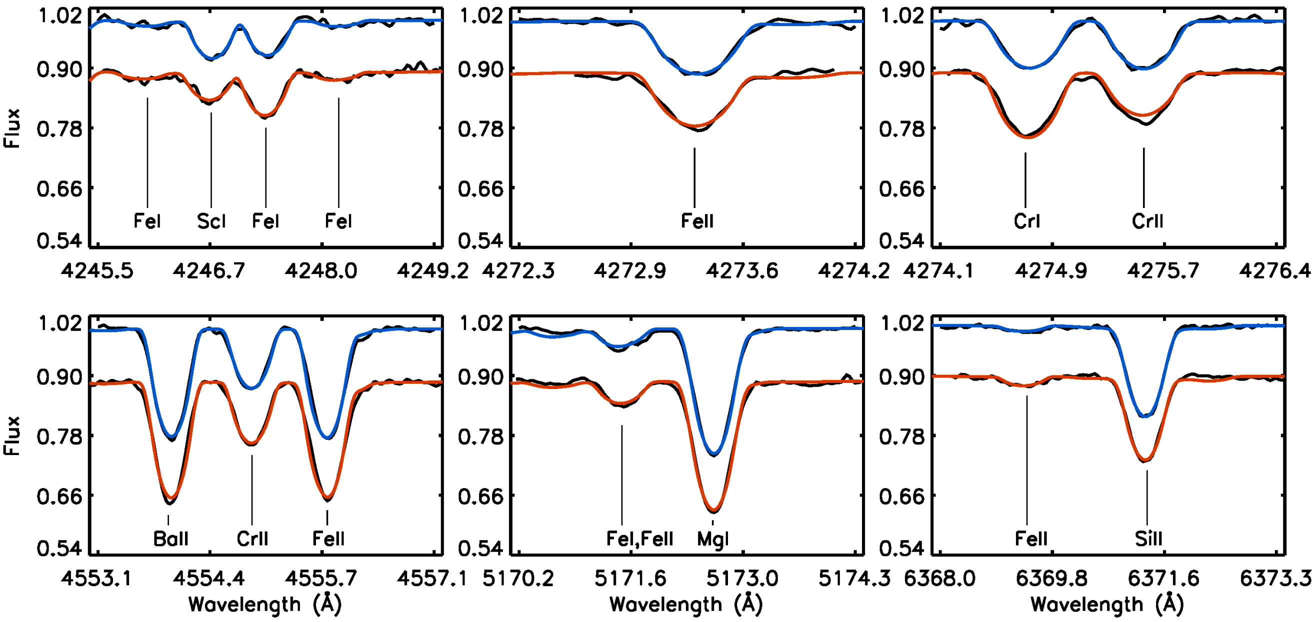

Fig. 8. Comparison of the observed (black lines) and theoretical spectra calculated for the final parameters. Star 1 is shown with the blue line, and Star 2 with the red line. The spectra of Star 2 were shifted by subtracting a value of 0.1 from the flux.

plain the frequency difference between the orbital frequency and the frequency of the spike if the core's synchronization has not yet been completed. However, this scenario is a bit questionable since both stars of 50 Dra are very slow rotators.

Trust et al. (2020) investigated 170 hump and spike stars containing normal A and Am/Fm stars. None of their sample stars has a spike frequency comparably small to that observed in 50 Dra components making our stars one of the slowest rotators among known hump and spike stars. This challenges the explanation of the hump and spike feature in 50 Dra and stresses the need to measure the strength of the magnetic field.

Regardless of the above mentioned, a possible explanation of the difference between the orbital frequency (and assumed synchronous rotation frequency of the stars) and the spike frequency would be anti-solar differential rotation. This is observed in some slowly rotating cool stars when the equatorial regions rotate more slowly than the polar regions (Rüdiger et al. 2019). In such a case, the polar regions would produce a higher frequency than the frequency of the synchronously rotating equatorial regions.

6.2. Chemical peculiarity

To check the chemical peculiarity/normality of 50 Dra components, we calculated average abundances of CP stars from the catalogue by Ghazaryan et al. (2018) and compared with abundances of both components listed in Table 5. The abundances of particular elements in AmFm (118 stars), HgMn (112) and ApBp (188) stars have typical uncertainties of 0.35, 0.65 and 0.60 dex, respectively. For stars with normal abundances, we used the compilation of 33 stars by Niemczura et al. (2017) with a typical uncertainty of the abundance value of 0.39 dex. In addition, we plot mean element abundances of 62 Am stars from Catanzaro et al. (2019, their table 3).

By comparing catalogue values with abundances of 50 Dra components listed in Table 5, we see that both stars follow the sequence of AmFm stars (Fig. 9), with low abundance of Sc and overabundant heavy and rare-earth elements. Note that the mean values of AmFm stars from Ghazaryan et al. (2018) are a bit different from those in Catanzaro et al. (2019) increasing the space of possible values for AmFm stars.

Previous studies have shown that more than 70 % of AmFm stars are part binary systems (e.g. Abt & Levy 1985; Carquillat & Prieur 2007). In addition, AmFm stars tend to appear in tight binaries with periods less than 20 days with a peak at about 5 days (Carquillat & Prieur 2007). It is believed that the tidal forces in binary systems play a crucial role in slowing down the rotation of these stars, which allows for atomic diffusion and the emergence of the chemical peculiarity observed in AmFm stars. In this context, 50 Dra is considered a typical representative of this class of CP stars.

Most of the Am stars have temperatures between 7250 and 8250 K peaking at 7750 K (Qin et al. 2019). From their collection of 9372 Am stars, Qin et al. (2019) found only 32 stars to have temperatures higher than 9000 K and only five to be hotter than 9500 K. On the other hand, Catanzaro et al. (2019) identified 15 out of their 62 Am sample stars to have temperatures above 9500 K based on SED fitting. Anyways, components of 50 Dra belong to a small group of hot Am stars.

7. Conclusions

We performed an analysis of twenty high-resolution spectra from the OES spectrograph (Koubský et al. 2004; Kabáth et al. 2020) together with photometric data from TESS (Ricker et al. 2015) to investigate 50 Dra. We modelled the radial velocity curve, as well as the photometric data to reveal that the system consists of two intermediate-mass stars with almost the same masses close to 2 $M_{\odot}$ ($q = 0.951$). The system with an or-

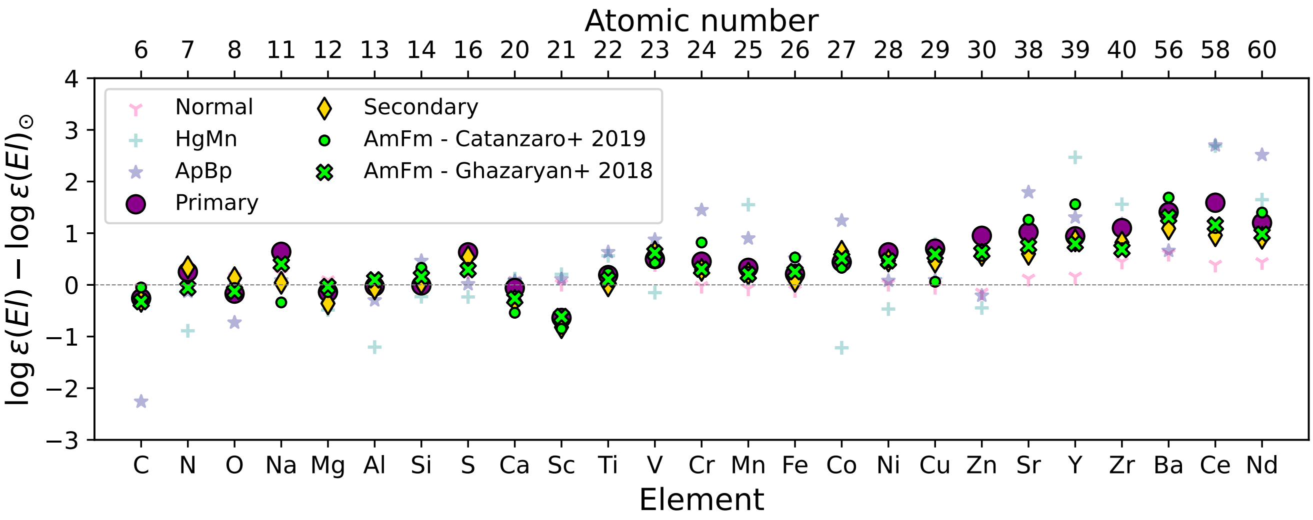

Fig. 9. Comparison of the mean element abundances of different classes of chemically peculiar stars (Ghazaryan et al. 2018; Catanzaro et al. 2019), normal stars (Niemczura et al. 2017) and 50 Dra components (magenta circles, yellow diamonds). The abundances of both stars of 50 Dra follow the AmFm abundances (green crosses and circles).

bital period of 4.117719(2) days is observed under an inclination of $i = 49.9(8)$ deg and shows ellipsoidal variations. Our investigation shows that both components are slow rotators with $v \sin i = 19(1)\,\mathrm{km\,s^{-1}}$ that rotate synchronously with the orbital period.

Based on the analysis of separated spectra and comparison with catalogue values, it was determined that both stars in the system are metallic-line AmFm CP stars with temperatures of 9800 and 9200 K. The high temperatures indicate that components of 50 Dra belong to a less common group of AmFm stars with temperatures higher than 9000 K. Apart from the effects of binarity, such as ellipsoidal variation, reflection effect, and beaming, the only feature detected in the frequency spectrum was a hump and spike around 0.275 c/d. No signs of p-mode pulsations or other variability were found. The frequency of the hump and spike feature is unusually low compared to other similar stars.

We were not able to assign the hump and spike feature to one of the components due to their similarities. We considered several possible explanations for this feature including Rossby modes (Saio et al. 2018), dynamo-generated magnetic fields producing spots (Cantiello & Braithwaite 2019), and overstable convection modes in the core (Lee & Saio 2020; Lee 2021). We also considered the possibility of anti-solar differential rotation, with polar regions rotating faster than equatorial regions. However, due to the high temperatures and slow rotation of both components, these explanations are uncertain and require further investigation. Specifically, one needs to measure the magnetic field strength and conduct detailed theoretical investigations of convection and dynamo-generated magnetic fields at these high temperatures and slow rotations. Additionally, an investigation of radiative diffusion and its role in producing the AmFm phenomenon in the presence of convection is desired.

Acknowledgements. MS acknowledges the support by Inter-transfer grant no LTT-20015. PK acknowledges the funding from ESA PRODEX PEA 4000127913. MS is grateful to T. van Reeth for the discussion about the nature of the additional variations and to P. Gajdoš for reading the manuscript. This paper includes data collected with the TESS mission. Funding for the TESS mission is provided by the NASA Explorer Program. Funding for the TESS Asteroseismic Science Operations Centre is provided by the Danish National Research Foundation (Grant agreement no.: DNRF106), ESA PRODEX (PEA 4000119301) and Stellar Astrophysics Centre (SAC) at Aarhus University. We thank the TESS team and staff and TASC/TASOC for their support of the present work. We also thank the TASC WG4 team for their contribution to the selection of targets for 2-minute observations. The TESS data were obtained from the MAST data archive at the Space Telescope Science Institute (STScI). We acknowledge the usage of the data taken with the Perek telescope at the Astronomical Institute of the Czech Academy of Sciences in Ondřejov and would like to thank the observers for their work. The calculations have been partly carried out using resources provided by the Wrocław Centre for Networking and Supercomputing (http://www.wcss.pl), Grant No 214. This research made use of NASA's Astrophysics Data System Bibliographic Services, and of the SIMBAD database, operated at CDS, Strasbourg, France.

References

Abt, H. A. 1961, ApJS, 6, 37
Abt, H. A. 1981, ApJS, 45, 437
Abt, H. A. & Levy, S. G. 1985, ApJS, 59, 229
Abt, H. A. & Morrell, N. I. 1995, ApJS, 99, 135
Antoci, V., Cunha, M., Houdek, G., et al. 2014, ApJ, 796, 118
Asplund, M., Grevesse, N., & Sauval, A. J. 2005, in Astronomical Society of the Pacific Conference Series, Vol. 336, Cosmic Abundances as Records of Stellar Evolution and Nucleosynthesis, ed. I. Barnes, Thomas G. & F. N. Bash, 25
Asplund, M., Grevesse, N., Sauval, A. J., & Scott, P. 2009, ARA&A, 47, 481
Balona, L. A. 2011, MNRAS, 415, 1691
Balona, L. A. 2013, MNRAS, 431, 2240
Balona, L. A., Baran, A. S., Daszyńska-Daszkiewicz, J., & De Cat, P. 2015, MNRAS, 451, 1445
Barentsen, G. & Lightkurve Collaboration. 2020, in American Astronomical Society Meeting Abstracts, Vol. 235, American Astronomical Society Meeting Abstracts #235, 409.04
Blazère, A., Neiner, C., & Petit, P. 2016a, MNRAS, 459, L81
Blazère, A., Petit, P., Lignières, F., et al. 2016b, A&A, 586, A97
Blazère, A., Petit, P., Neiner, C., et al. 2020, MNRAS, 492, 5794
Bressan, A., Marigo, P., Girardi, L., et al. 2012, MNRAS, 427, 127
Cantiello, M. & Braithwaite, J. 2019, ApJ, 883, 106
Carquillat, J. M. & Prieur, J. L. 2007, MNRAS, 380, 1064
Catanzaro, G., Busà, I., Gangi, M., et al. 2019, MNRAS, 484, 2530
Catanzaro, G., Frasca, A., Alonso-Santiago, J., & Colombo, C. 2024, A&A, 685, A133
Charbonneau, P. & Michaud, G. 1991, ApJ, 370, 693
Claret, A. 2003, A&A, 406, 623
Claret, A., Cukanovaite, E., Burdge, K., et al. 2020, A&A, 641, A157
Claret, A. & Gimenez, A. 1989, A&AS, 81, 37
Conroy, K. E., Kochoska, A., Hey, D., et al. 2020, ApJS, 250, 34
Cutri, R. M., Skrutskie, M. F., van Dyk, S., et al. 2003, VizieR Online Data Catalog: 2MASS All-Sky Catalog of Point Sources (Cutri+ 2003), VizieR On-line Data Catalog: II/246. Originally published in: 2003yCat.2246....0C

Cutri, R. M., Wright, E. L., Conrow, T., et al. 2021, VizieR Online Data Catalog: AllWISE Data Release (Cutri+ 2013), VizieR On-line Data Catalog: II/328. Originally published in: IPAC/Caltech (2013)
da Silva, L., Girardi, L., Pasquini, L., et al. 2006, A&A, 458, 609
Eker, Z., Bakış, V., Bilir, S., et al. 2018, MNRAS, 479, 5491
Gaia Collaboration, Brown, A. G. A., Vallenari, A., et al. 2018, A&A, 616, A1
Gaia Collaboration, Brown, A. G. A., Vallenari, A., et al. 2021, A&A, 649, A1
Gaia Collaboration, Vallenari, A., Brown, A. G. A., et al. 2023, A&A, 674, A1
Ghazaryan, S., Alecian, G., & Hakobyan, A. A. 2018, MNRAS, 480, 2953
Gontcharov, G. A. 2006, Astronomy Letters, 32, 759
Gray, R. O., Corbally, C. J., De Cat, P., et al. 2016, AJ, 151, 13
Hadrava, P. 1995, A&AS, 114, 393
Hadrava, P. 2004, Publications of the Astronomical Institute of the Czechoslovak Academy of Sciences, 92, 15
Harper, W. E. 1919, JRASC, 13, 236
Henriksen, A. I., Antoci, V., Saio, H., et al. 2023a, MNRAS, 520, 216
Henriksen, A. I., Antoci, V., Saio, H., et al. 2023b, MNRAS, 524, 4196
Høg, E., Fabricius, C., Makarov, V. V., et al. 2000, A&A, 355, L27
Huang, C. X., Vanderburg, A., Pál, A., et al. 2020a, Research Notes of the American Astronomical Society, 4, 204
Huang, C. X., Vanderburg, A., Pál, A., et al. 2020b, Research Notes of the American Astronomical Society, 4, 206
Husser, T.-O., Wende-von Berg, S., Dreizler, S., et al. 2013, A&A, 553, A6
Hut, P. 1980, A&A, 92, 167
Jenkins, J. M., Twicken, J. D., McCauliff, S., et al. 2016, in Society of Photo-Optical Instrumentation Engineers (SPIE) Conference Series, Vol. 9913, Software and Cyberinfrastructure for Astronomy IV, ed. G. Chiozzi & J. C. Guzman, 99133E
Kabáth, P., Skarka, M., Sabotta, S., et al. 2020, PASP, 132, 035002
Kochukhov, O., Adelman, S. J., Gulliver, A. F., & Piskunov, N. 2007, Nature Physics, 3, 526
Kochukhov, O., Gürsoytrak Mutlay, H., Amarsi, A. M., et al. 2023, MNRAS, 521, 3480
Kochukhov, O., Khalack, V., Kobzar, O., et al. 2021, MNRAS, 506, 5328
Koubský, P., Mayer, P., Čáp, J., et al. 2004, Publications of the Astronomical Institute of the Czechoslovak Academy of Sciences, 92, 37
Kurucz, R. L. 2005, Memorie della Societa Astronomica Italiana Supplementi, 8, 14
Lee, U. 2021, MNRAS, 505, 1495
Lee, U. & Saio, H. 2020, MNRAS, 497, 4117
Lightkurve Collaboration, Cardoso, J. V. d. M., Hedges, C., et al. 2018, Lightkurve: Kepler and TESS time series analysis in Python, Astrophysics Source Code Library
Michaud, G. 1970, ApJ, 160, 641
Murphy, S. J., Saio, H., Takada-Hidai, M., et al. 2020, MNRAS, 498, 4272
Nguyen, C. T., Costa, G., Girardi, L., et al. 2022, A&A, 665, A126
Niemczura, E., Murphy, S. J., Smalley, B., et al. 2015, MNRAS, 450, 2764
Niemczura, E., Polińska, M., Murphy, S. J., et al. 2017, MNRAS, 470, 2870
Ogilvie, G. I. 2014, ARA&A, 52, 171
Paegert, M., Stassun, K. G., Collins, K. A., et al. 2021, arXiv e-prints, arXiv:2108.04778
Paunzen, E. 2015, A&A, 580, A23
Petit, P., Lignières, F., Aurière, M., et al. 2011, A&A, 532, L13
Preston, G. W. 1971, PASP, 83, 571
Preston, G. W. 1974, ARA&A, 12, 257
Pych, W. 2004, PASP, 116, 148
Qin, L., Luo, A. L., Hou, W., et al. 2021, AJ, 162, 32
Qin, L., Luo, A. L., Hou, W., et al. 2019, ApJS, 242, 13
Reinhold, T. & Gizon, L. 2015, A&A, 583, A65
Ricker, G. R., Winn, J. N., Vanderspek, R., et al. 2015, Journal of Astronomical Telescopes, Instruments, and Systems, 1, 014003
Rodrigues, T. S., Bossini, D., Miglio, A., et al. 2017, MNRAS, 467, 1433
Rodrigues, T. S., Girardi, L., Miglio, A., et al. 2014, MNRAS, 445, 2758
Royer, F., Zorec, J., & Gómez, A. E. 2007, A&A, 463, 671
Rüdiger, G., Küker, M., Käpylä, P. J., & Strassmeier, K. G. 2019, A&A, 630, A109
Saio, H., Kurtz, D. W., Murphy, S. J., Antoci, V. L., & Lee, U. 2018, MNRAS, 474, 2774
Sbordone, L. 2005, Memorie della Societa Astronomica Italiana Supplementi, 8, 61
Sikora, J., David-Uraz, A., Chowdhury, S., et al. 2019, MNRAS, 487, 4695
Skarka, M., Žák, J., Fedurco, M., et al. 2022, A&A, 666, A142
Smalley, B., Antoci, V., Holdsworth, D. L., et al. 2017, MNRAS, 465, 2662
Tody, D. 1986, in Society of Photo-Optical Instrumentation Engineers (SPIE) Conference Series, Vol. 627, Instrumentation in astronomy VI, ed. D. L. Crawford, 733
Trust, O., Jurua, E., De Cat, P., & Joshi, S. 2020, MNRAS, 492, 3143
Twicken, J. D., Chandrasekaran, H., Jenkins, J. M., et al. 2010, in Society of Photo-Optical Instrumentation Engineers (SPIE) Conference Series, Vol. 7740, Software and Cyberinfrastructure for Astronomy, ed. N. M. Radziwill & A. Bridger, 77401U
Vines, J. I. & Jenkins, J. S. 2022, MNRAS[`arXiv:2204.03769`]
Wilson, R. E. 1953, Carnegie Institute Washington D.C. Publication, 0
Zorec, J. & Royer, F. 2012, A&A, 537, A120
Zucker, S., Mazeh, T., & Alexander, T. 2007, ApJ, 670, 1326

Table A.1. Stars in the vicinity of 50 Dra shown in Fig. 2.

NR	Gaia DR3 ID	G	B-R
1	2268466696271988736	13.047	0.9704
2	2268467349107014400	13.72	0.971
3	2268467383466749184	14.873	0.951
4	2268467349107013760	15.786	1.3158
5	2268466627552513024	16.034	1.0765
6	2268467894567507072	16.153	1.1483
7	TIC 335965559	16.331	-
8	2268467898862831360	16.407	0.9278
9	2268467795783608832	16.5	1.4393
10	2268466661912250752	16.529	1.8639
11	2268467074229113344	16.703	1.0081
12	TIC 335965560	17.059	-
13	2268467727064133248	17.088	1.0404
14	2268467928927245952	17.624	0.8851
15	2268467757127995264	17.681	1.0049
16	2268467379171426048	17.767	1.2799
17	2268467688408453248	17.856	2.0393

Notes. Data from Gaia Collaboration et al. (2023)

Table A.2. Pulsation frequencies detected in the data.

f (c/d)	a (mmag)	n	f (c/d)	a (mmag)	n
0.233 06(5)	0.03(1)	1	0.270 51(2)	0.08(1)	2
0.235 22(4)	0.09(1)	1	0.271 10(2)	0.13(2)	2
0.236 35(5)	0.12(1)	1	0.273 05(2)	0.24(2)	2
0.237 61(4)	0.14(1)	2	0.273 53(1)	0.24(1)	2
0.238 82(4)	0.10(1)	2	0.275 08(1)	0.41(2)	2
0.241 13(3)	0.10(1)	1	0.275 73(1)	0.26(2)	2
0.242 25(4)	0.07(1)	1	0.276 29(1)	0.18(1)	2
0.248 11(3)	0.15(1)	2	0.276 91(1)	0.11(1)	2
0.249 40(3)	0.17(2)	2	0.280 46(2)	0.15(1)	2
0.250 54(5)	0.08(2)	1	0.281 64(3)	0.12(1)	2
0.252 80(4)	0.10(2)	2	0.285 38(4)	0.07(1)	2
0.255 12(4)	0.12(2)	2	0.286 97(7)	0.04(1)	1
0.256 30(2)	0.15(2)	1	0.289 18(6)	0.06(1)	1
0.260 60(4)	0.06(1)	1	0.290 72(3)	0.08(1)	1
0.263 71(8)	0.13(3)	1	0.295 14(7)	0.02(1)	1
0.263 99(3)	0.18(3)	2	0.298 20(4)	0.04(1)	1
0.266 07(1)	0.25(1)	1	0.302 08(4)	0.04(1)	1
0.268 67(1)	0.33(1)	1	0.306 45(4)	0.04(1)	1
0.269 93(2)	0.11(2)	2	0.308 20(5)	0.02(1)	1

Notes. Column ‘n’ gives the number of harmonics, despite the frequencies are mostly unresolved.

Appendix A: Supporting material

Table A.3. Magnitudes used for SED fitting.

Filter	Magnitude	Uncertainty	Ref
STROMGREN v	5.598	0.013	1
STROMGREN b	5.392	0.006	1
GaiaDR2v2 BP	5.371	0.003	2
STROMGREN y	5.369	0.001	1
GaiaDR2v2 G	5.357	0.003	2
GaiaDR2v2 RP	5.303	0.006	2
TESS T	5.345	0.007	3
2MASS J	5.219	0.018	4
2MASS H	5.233	0.031	4
2MASS Ks	5.206	0.018	4
WISE RSR $W1$	5.249	0.188	5
WISE RSR $W2$	5.092	0.071	5

Notes. References: 1 – Paunzen (2015), 2 – Gaia Collaboration et al. (2018), 3 – Paegert et al. (2021), 4 – Cutri et al. (2003), 5 – Cutri et al. (2021)